



HAL
open science

Ion Kinetics in a Hot Flow Anomaly: MMS Observations

Steven Schwartz, Levon Avanov, Drew Turner, Hui Zhang, Imogen Gingell,
Jonathan P Eastwood, Daniel J Gershman, Andreas Johlander, Christopher
Russell, James Burch, et al.

► **To cite this version:**

Steven Schwartz, Levon Avanov, Drew Turner, Hui Zhang, Imogen Gingell, et al.. Ion Kinetics in a Hot Flow Anomaly: MMS Observations. *Geophysical Research Letters*, 2018, 10.1029/2018GL080189 . hal-02372783

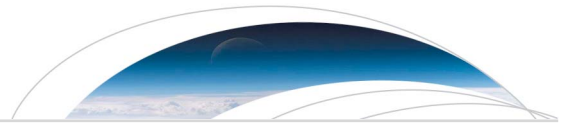
HAL Id: hal-02372783

<https://hal.science/hal-02372783v1>

Submitted on 20 Nov 2019

HAL is a multi-disciplinary open access archive for the deposit and dissemination of scientific research documents, whether they are published or not. The documents may come from teaching and research institutions in France or abroad, or from public or private research centers.

L'archive ouverte pluridisciplinaire **HAL**, est destinée au dépôt et à la diffusion de documents scientifiques de niveau recherche, publiés ou non, émanant des établissements d'enseignement et de recherche français ou étrangers, des laboratoires publics ou privés.



RESEARCH LETTER

10.1029/2018GL080189

Key Points:

- MMS observations reveal distinct ion velocity-space populations within a Hot Flow Anomaly (HFA)
- The HFA interior varies smoothly in density with a swept-up pressure excess toward the trailing edge
- The HFA interior displays coherent kinematic coupling between antisunward and sunward backstreaming ions

Supporting Information:

- Supporting Information S1

Correspondence to:

S. J. Schwartz,
stevan.schwartz@asp.colorado.edu

Citation:

Schwartz S. J., Avinov, L., Turner, D., Zhang, H., Gingell, I., Eastwood, J. P., et al. (2018). Ion kinetics in a hot flow anomaly: MMS observations. *Geophysical Research Letters*, 45, 11,520–11,529. <https://doi.org/10.1029/2018GL080189>

Received 23 AUG 2018

Accepted 14 OCT 2018

Accepted article online 19 OCT 2018

Published online 4 NOV 2018

Ion Kinetics in a Hot Flow Anomaly: MMS Observations

Steven J Schwartz^{1,2}, Levon Avinov³, Drew Turner⁴, Hui Zhang⁵, Imogen Gingell¹, Jonathan P Eastwood¹, Daniel J Gershman³, Andreas Johlander⁶, Christopher T Russell⁷, James L Burch⁸, John C Dorelli³, Stefan Eriksson², Robert E Ergun², Stephen A Fuselier^{8,9}, Barbara L Giles³, Katherine A Goodrich², Yuri V Khotyaintsev⁶, Benoit Lavraud^{1,10}, Per-Arne Lindqvist⁶, Mitsuo Oka^{1,11}, Tai-Duc Phan^{1,11}, Robert J Strangeway⁷, Karlheinz J Trattner², Roy B Torbert^{1,2,12}, Andris Vaivads⁶, Hanying Wei⁷, and Frederick Wilder²

¹Imperial College London, London, UK, ²Laboratory for Atmospheric and Space Physics, University of Colorado Boulder, Boulder, CO, USA, ³NASA, Goddard Space Flight Center, Greenbelt, MD, USA, ⁴The Aerospace Corporation, Los Angeles, CA, USA, ⁵Geophysical Institute, University of Alaska Fairbanks, Fairbanks, AK, USA, ⁶Swedish Institute of Space Physics (Uppsala), Uppsala, Sweden, ⁷Earth Planetary and Space Sciences, University of California, Los Angeles, CA, USA, ⁸Southwest Research Institute, San Antonio, TX, USA, ⁹Department of Physics & Astronomy, University of Texas at San Antonio, San Antonio, TX, USA, ¹⁰Institut de Recherche en Astrophysique et Planétologie, CNRS, UPS, CNES, Université de Toulouse, Toulouse, France, ¹¹Space Sciences Laboratory, University of California, Berkeley, CA, USA, ¹²Department of Physics, University of New Hampshire, Durham, NH, USA

Abstract Hot Flow Anomalies (HFAs) are transients observed at planetary bow shocks, formed by the shock interaction with a convected interplanetary current sheet. The primary interpretation relies on reflected ions channeled upstream along the current sheet. The short duration of HFAs has made direct observations of this process difficult. We employ high resolution measurements by NASA’s Magnetospheric Multiscale Mission to probe the ion microphysics within a HFA. Magnetospheric Multiscale Mission data reveal a smoothly varying internal density and pressure, which increase toward the trailing edge of the HFA, sweeping up particles trapped within the current sheet. We find remnants of reflected or other backstreaming ions traveling along the current sheet, but most of these are not fast enough to out-run the incident current sheet convection. Despite the high level of internal turbulence, incident and backstreaming ions appear to couple gyro-kinetically in a coherent manner.

Plain Language Summary Shock waves in space are responsible for energizing particles and diverting supersonic flows around planets and other obstacles. Explosive events known as Hot Flow Anomalies (HFAs) arise when a rapid change in the interplanetary magnetic field arrives at the bow shock formed by, for example, the supersonic solar wind plasma flow from the Sun impinging on the Earth’s magnetic environment. HFAs are known to produce impacts all the way to ground level, but the physics responsible for their formation occur too rapidly to be resolved by previous satellite missions. This paper employs NASA’s fleet of four Magnetospheric Multiscale satellites to reveal for the first time clear, discreet populations of ions that interact coherently to produce the extreme heating and deflection.

1. Introduction

The bow shock formed by the impact of the supermagnetosonic solar wind upon the Earth’s magnetosphere has been the primary research laboratory for shock waves in collisionless plasmas. In addition to slowing, deflecting, and heating the incident flow, the shock contends with multiple particle species and plasma fluctuations, giving rise to nonthermal processes including selective acceleration of particles to high energies, growth of instabilities, and development of non-Maxwellian particle distributions. See Paschmann et al. (2005), Tsurutani and Stone (1985), and Burgess and Scholer (2015).

The interplanetary magnetic field orientation plays a central role in bow shock physics. Under quasi-perpendicular geometries, in which the angle θ_{Bn} between the field and shock normal is $>45^\circ$, and Alfvén Mach numbers $\gtrsim 3$, quasi-perpendicular shocks are *supercritical*. Some incident solar wind ions reflect and subsequently gyrate into the downstream region. This mechanism turns directed bulk flow energy into

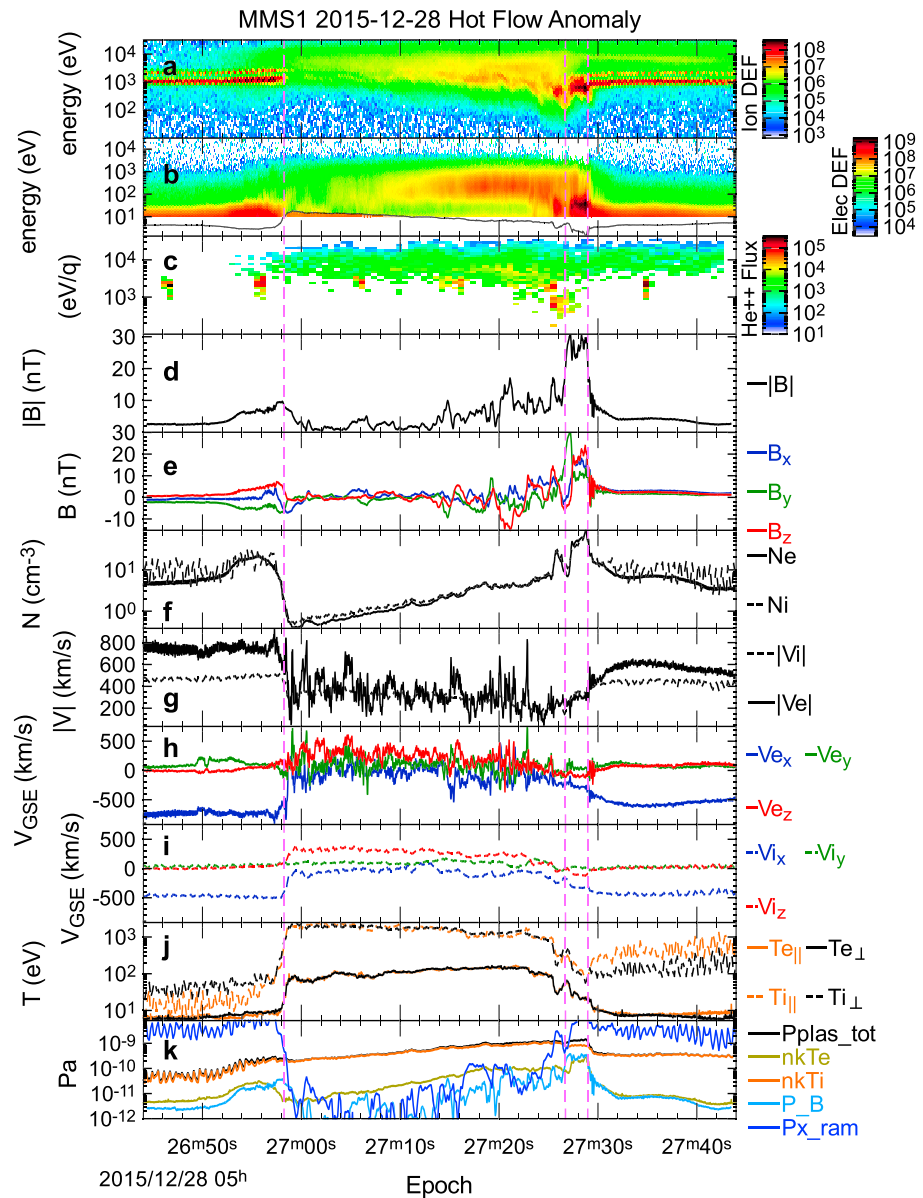


Figure 1. MMS1 overview of the Hot Flow Anomaly. (a) ion and (b) electron omnidirectional differential energy fluxes [keV/(cm²·s·sr·keV)] over-plotted with spacecraft potential (black line), (c) alpha particle flux [1/(cm²·s·sr·eV)], (d) magnetic field strength and (e) GSE components, (f) electron and ion number densities, (g) bulk speeds and (h,i) GSE flow components, (j) electron and ion temperatures parallel and perpendicular to **B**, and (k) thermal, magnetic, and total pressures and ρV_x^2 ram pressure. Due to instrumental limitations in the solar wind (see supporting information S1), the thermal pressures shown in panel (k) are unreliable in the solar wind before and after the Hot Flow Anomaly; see values from the WIND spacecraft in Table 1. Dashed vertical lines denote the leading inner edge, trailing inner edge, and trailing compression. MMS = Magnetospheric Multiscale Mission.

internal energy. Under quasi-parallel geometries ($\theta_{Bn} \lesssim 45^\circ$) some particles can escape upstream forming an extended turbulent foreshock populated by suprathermal ions.

Hot Flow Anomalies (HFAs) are the result of interplanetary current sheets changing the field orientation over kinetic scales at the bow shock (Paschmann et al., 1988; Schwartz et al., 1985, 2000; Thomsen et al., 1986, 1988). They have hot interiors containing flow strongly deflected from the antisunward direction; the over-pressure causes HFA expansion, driving shocks at one or both edges. Burgess (1989) demonstrated a mechanism (Burgess & Schwartz, 1988) in which ions reflected under quasi-perpendicular conditions were channeled upstream by the changing geometry. This process involves interplanetary $-\mathbf{V} \times \mathbf{B}$ electric fields which point

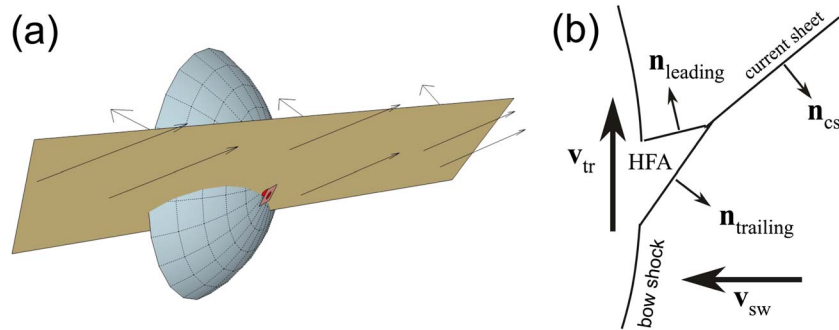


Figure 2. (a) Sketch of the bow shock-interplanetary current sheet interaction. Arrows show the solar wind magnetic field directions on either side. (b) 2-D schematic of the intersection of the interplanetary current sheet with the bow shock showing the approximate orientations of the leading and trailing edges. The structure appears to transit along the shock front at \mathbf{V}_{tr} due to the convection of the current sheet by the incoming solar wind. Table 1 estimates the HFA size as $2.3 R_E$ along the shock and $1 R_E$ sunward from the nominal shock surface. HFA = Hot Flow Anomaly.

toward the current sheet on at least one side (Thomsen et al., 1993). Simulations (Burgess & Schwartz, 1988; Omidi & Sibeck, 2007) support this scenario although statistical studies (Wang et al., 2013; Zhao et al., 2017b) show that HFA-like signatures are found under wider conditions.

HFAs can have a significant impact on the magnetopause (Sibeck et al., 2000, 1999), producing disturbances throughout the magnetosphere to the ground (Eastwood et al., 2008, 2011; Hartinger et al., 2013; Zhao et al., 2017a). They have been observed at the bow shocks of Mercury (Uritsky et al., 2014), Venus (Collinson et al., 2014, 2015), Mars (Collinson et al., 2012), Jupiter (Valek et al., 2017), and Saturn (Masters et al., 2008, 2009). They are frequent (>3 per day, Facskó et al., 2008, 2009; Schwartz et al., 2000; ~7 can be observed within a 12-hr interval, Zhang et al., 2010).

HFAs are typically a few minutes in duration. *Mature HFAs* have hot interior regions, with a single ion component and near-Maxwellian electron distributions (Thomsen et al., 1988). *Young HFAs* have central regions in which the solar wind beam is distinct from counter-streaming ions (Lucek et al., 2004; Shestakov & Vaisberg, 2016; Zhang et al., 2010) which may be of magnetosheath origin (Vaisberg et al., 2016), although the central temperatures are often too high to be explained by a simple conversion of solar wind kinetic energy (Onsager et al., 1990; Wang et al., 2013).

Recent work (Liu et al., 2017; Turner et al., 2018) explored the energetic particle populations at HFAs. Past work on HFA formation and heating mechanisms has utilized higher-resolution electromagnetic field data, with particle information accumulated over ~3–4 s. Consequently, many details, including proposed turbulent versus coherent heating and energization mechanisms, are not well resolved. We take advantage of the high resolution full 3-D velocity-space particle data taken by NASA's Magnetospheric Multiscale Mission (MMS; Burch et al., 2016) to study this microphysics.

2. Data

2.1. Instruments

We study a HFA that was captured in burst mode on 28 December 2015 at 05:27 UT. Fast Plasma Investigation (FPI) electron (ion) measurements have 30 (150) ms cadences (Pollock et al., 2016). The excellent agreement of the electron and ion densities here suggests that the HFA interior is very well-characterized by the measurements, although FPI is not able to capture accurately the cold, low density solar wind plasma with the same accuracy (see supporting information S1). Fields data (Torbert et al., 2016) including Fluxgate Magnetometer (FGM) magnetic field (Russell et al., 2016) at 128 vectors per second are used together with electric field measurements derived from the spin-plane (Lindqvist et al., 2016) and axial (Ergun et al., 2016) booms. The Hot Plasma Composition Analyzer (HPCA; Young et al., 2016) provides alpha particle data.

2.2. Event Overview

Figure 1 presents an overview of the HFA plasma and field data. The current sheet-bow shock intersection moves northward as it convects with the solar wind. The orientation of the leading (Earthward) edge at 05:26:52 UT is sketched in Figure 2. Figure 2b shows the high inclination of the current sheet, exaggerated by

Table 1
Solar Wind Conditions and Current Sheet/HFA Parameters

Parameter	Value	Units
Spacecraft position	(11.1, -4.1, -1.1)	R_E (GSE)
Model bow shock normal ^a	(0.974, -0.219, -0.054)	GSE
β_i	2.3	<pre, post> _{avg}
$V_{A,CS}$	21, 29	km/s <pre, post> _{avg}
M_{An}, M_{ms}	23, 14	Shock Mach numbers <pre,post> _{avg}
Pre-event conditions	05:26:44.000–05:26:49.357	
\mathbf{B}_{pre}	(-0.824, -2.24, 0.708)	nT (GSE)
$ \mathbf{B}_{pre} $	2.5	nT
$\theta_{Bn\ pre}$	98 (82)	Degrees
$n_{p\ pre}$ (WIND)	8.1	cm ⁻³
\mathbf{V}_{pre} (WIND)	(-481, 12, -12)	km/s (GSE)
$T_{p\ pre}$ (WIND)	4	eV
$\mathbf{E}_{pre} = -\mathbf{V} \times \mathbf{B}$	(19, -350, -1100)	$\mu\text{V/m}$ (GSE)
Post-event conditions	05:27:39.712–05:27:43.608	
\mathbf{B}_{post}	(1.95, 1.17, 1.38)	nT (GSE)
$ \mathbf{B}_{post} $	2.7	nT
$\theta_{Bn\ post}$	54°	Degrees
$n_{p\ post}$ (WIND)	6	cm ⁻³
\mathbf{V}_{post} (WIND)	(-495, 3, -18)	km/s (GSE)
$T_{p\ post}$ (WIND)	6	eV
$\mathbf{E}_{post} = -\mathbf{V} \times \mathbf{B}$	(-30, -650, 600)	$\mu\text{V/m}$ (GSE)
Current sheet/HFA parameters		
Current sheet normal, \mathbf{n}_{CS}	(0.680, -0.437, -0.590)	GSE ($\mathbf{B}_{post} \times \mathbf{B}_{pre}$)
$V_{nCS} \equiv \mathbf{V}_{sw} \cdot \mathbf{n}_{CS}$	-325	km/s
$\theta_{BpreBpost}$	120°	Degrees (magnetic shear angle)
$\mathbf{E}_{pre} \cdot \mathbf{n}_{CS}$	+810	$\mu\text{V/m}$ (\Rightarrow toward CS)
$\mathbf{E}_{post} \cdot \mathbf{n}_{CS}$	-80	$\mu\text{V/m}$ (\Rightarrow toward CS)
$\mathbf{n}_{leading}$	(-0.340, 0.633, 0.696)	4SC timing (inner edge)
$\mathbf{n}_{trailing}$	(0.861, 0.007, -0.508)	4SC timing (trailing shock)
$V_{n\ leading}$	234	km/s (4SC timing)
$V_{n\ trailing}$	-166	km/s (4SC timing)
$\Delta\mathbf{V}(trailing - leading) \cdot \mathbf{n}_{CS}$	68	km/s (HFA expansion)
$\theta_{Bn\ trailing}$	68	Degrees
\mathbf{V}_{tr}^b	(77, 228, 473)	GSE km/s (CS track along shock)
$ \mathbf{V}_{tr}/V_g _{pre \cdot post}$	0.6, 0.7	Ratio transit speed to gyration
Size ($V_{tr} \times 28$ s duration)	2.3	R_E
Extent upstream	1.0	R_E (to leading/trailing intersection)
Age	218	s (size/expansion speed)
Distance from birth	< 18	R_E (age $\times \mathbf{V}_{tr} $)

Note. HFA = Hot Flow Anomaly.

^aUses dayside empirical fit by Slavin and Holzer (1981). See also Schwartz (1998). ^bSchwartz et al. (2000).

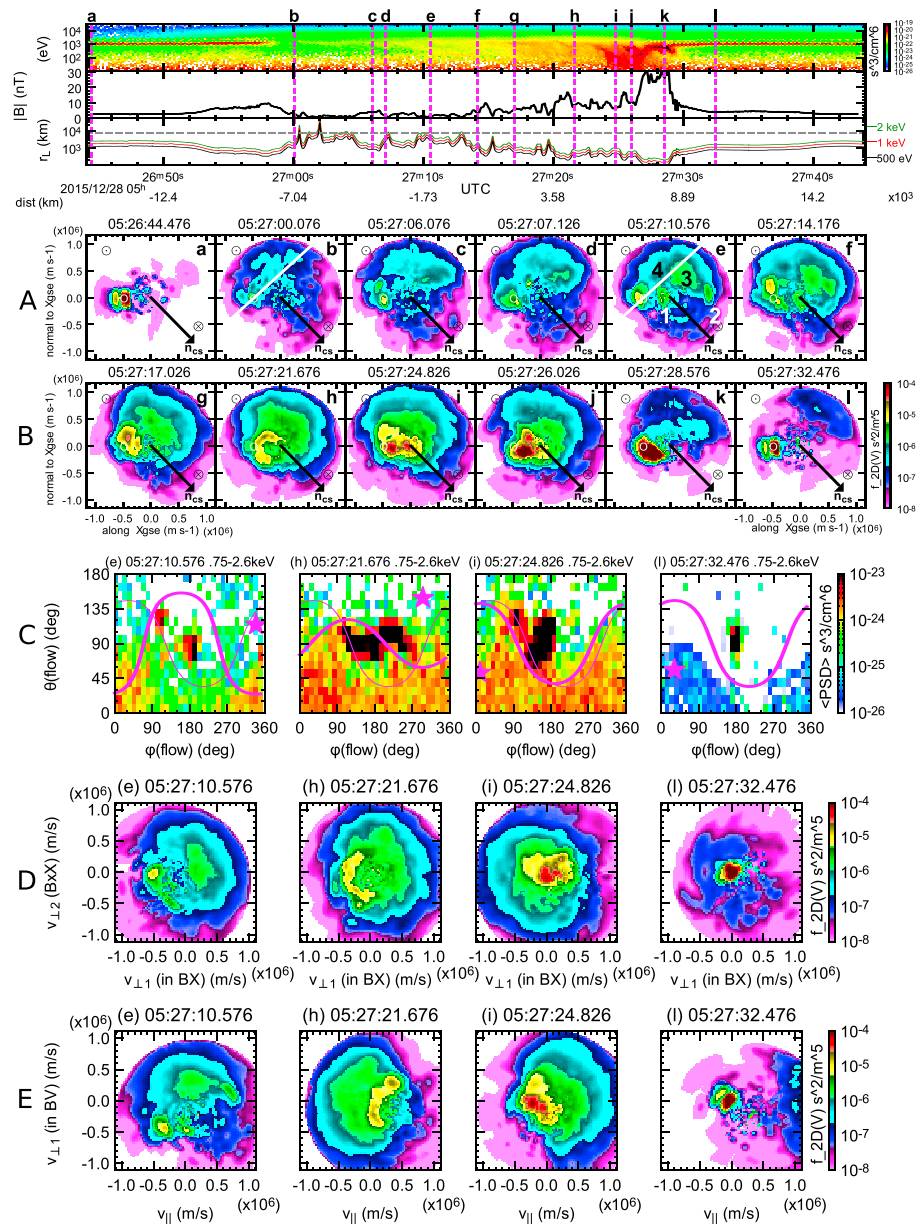


Figure 3. MMS1 reduced ion distributions. (Top) omnidirectional spectrograms, magnetic field magnitude, gyroradii of protons in the local, 2.5 s smoothed magnetic field. The dashed line is the HFA half-thickness. (A–B) FPI phase-space distributions reduced by cartesian integration onto the X_{GSE} — (horizontal) current sheet normal (black arrow) plane. The circled dot and cross show the out-of-plane magnetic field component pre- and post-HFA. Letters correspond to times of each distribution indicated above the time series panel. The white lines in pane A(b,e) are velocities with zero component along the current sheet normal in a frame convecting with the current sheet. (C) Polar versus azimuthal angle skymaps. The thick magenta line represents 90° pitch angles in the spacecraft frame based on the local magnetic field direction, with a star indicating the tip of the field vector. The thin magenta line is the same but based on the post-HFA field direction. (D–E) Reduced distributions shifted to their bulk velocity frame and integrated onto the (D) $v_{\perp} - v_{\perp}$ and (E) $v_{\perp} - v_{\parallel}$ planes. HFA = Hot Flow Anomaly.

the inclination of the leading edge based on 4-spacecraft timing of the inner boundary (see $\mathbf{n}_{leading}$ in Table 1), that results in a weak northward and antisunward compression (see Lucek et al., 2004, Figure 3) predominantly transverse to the Sun-Earth line.

The trailing edge shows a strong sunward magnetic compression (Figure 2d) associated with a high Mach number shock (Fuselier et al., 1987). The compression magnitude is similar to the bow shock crossing 2 min

later (Figure S2). The orientation of this edge (Figure 2b) is sunward and southward. It will relax to the nominal bow shock position as the current sheet-bow shock intersection tracks northward.

There is a clear pre- to post-HFA change in interplanetary field orientation (see Figure 2a and Table 1). The interior density depression (Figure 1f) is followed by a gradual rise toward the trailing edge compression. This depression, by an order of magnitude from solar wind values, is much greater than the relative magnetic field depression ~ 2.5 . Thus, in addition to the 2-D expansion transverse to \mathbf{B} there must be some expansion, for example, along the current sheet. The HFA interior is hot (Figure 2j) and shows significant flow deflection (Figures 2h and 2i), primarily in the $+z$ direction, consistent with the overall HFA motion, and deceleration in x .

Table 1 summarizes the HFA and solar wind conditions. The geometry of the bow shock and interplanetary current sheet control HFA formation and evolution (Paschmann et al., 1988; Schwartz et al., 1985, 1988; Thomsen et al., 1988). Figure 2a sketches the current sheet orientation based on the cross product between the pre- and post-HFA magnetic fields and assuming the sheet is a tangential discontinuity. Figure 2b shows the orientations of the leading and trailing edges.

Schwartz et al. (2000) introduced the ratio $|V_{tr}/V_g|$ between the velocity of the bow shock-current sheet intersection point and the gyro-velocity of a specularly reflected ion. Table 1 shows that this ratio is small enough to give ions reflected at the shock access to the current sheet before convection moves it too far along the shock. The orientation of the solar wind $-\mathbf{V} \times \mathbf{B}$ electric field points toward the current sheet on both sides, bringing bow shock-reflected ions toward, rather than away from, the current sheet.

The leading and trailing edge speeds and orientations given in Table 1 were calculated based on four spacecraft timing analysis (e.g., Schwartz, 1998). Projecting the difference between these two edge velocities along the underlying current sheet normal provides an estimate of the HFA expansion speed of 68 km/s, similar to other reported values (Liu et al., 2016; Schwartz et al., 1985).

Table 1 also shows calculations of the HFA extent $\sim 2.3 R_E$ along the bow shock. From the intersection of the two edges, the HFA projects $\sim 1 R_E$ upstream. Table 1 calculates the HFA age and distance from its birth.

3. Results and Discussion

3.1. Ion Kinetics—Early Interior

Figures 3A–3B show ion distributions observed at locations within the HFA, reduced by cartesian integration onto the plane containing the GSE x axis and current sheet normal. This orientation matches qualitatively that of Figures 2a and 2b. Figures 3D–3E are similar integrations onto planes related to the magnetic field (see caption and axis labels). Figure 3A(a) shows the pre-event solar wind beam traveling at $V_x \approx -500$ km/s. The solar wind alpha particles appear as a second peak at $V_x \approx -650$ km/s. This region of velocity space is populated throughout much of the HFA. The white line in Figure 3A(b,e) (omitted elsewhere for clarity) indicates velocities tangential to the current sheet in a frame convecting with it. Particles traveling upstream within the current sheet will lie near the sunward (right) portion of this line.

On HFA entry (Figure 3A(b)), peaks remain at the solar wind proton and alpha locations, reduced significantly in density. Figure 3A(b) shows an extended population with velocities along the convecting current sheet (along the white line). This extended population may originate from deeper in the HFA or magnetosheath (Vaisberg et al., 2016).

The solar wind beam persists through the first half of the HFA (row (A)) with only modest spreading and deflection. It is accompanied by three distinct groups of ions and a broader population (see numbers in Figure 3A(e)):

1. A low energy population toward the center of the panes (cf. Figure 3A(d)), progressing from the white line to velocities with a component along the current sheet normal (Figure 3A(e,f)), that is, southward and sunward relative to the convecting current sheet. This distinct group may have its origins in ions reflected by the bow shock and channeled along the current sheet as proposed by Burgess (1989).
2. A tight bunch traveling in the $+X_{GSE}$ direction with speeds ~ 500 – 700 km/s most notable in Figure 3A(e). These may be newly reflected solar wind protons. From C(e) we see that these are close to the broader population discussed below occupying the lower portion of the sky map, most intense near $0^\circ/360^\circ$ azimuths. Figures 3D–3E(e) reveal that these ions are not organized by the local magnetic field, consistent with their large gyroradii in the early portion of the HFA (see the third panel at the top).

3. A more dispersed sunward population with speeds comparable to the solar wind that peaks below the convection locus. This population is drifting toward the trailing edge of the HFA and may have been reflected earlier than group (2).
4. However, it is attached to a broader population that fills the upper portion of the panes, connecting smoothly onto the antisunward solar wind peak. From Figure 3D(e) we see that these ions, together with the remnant of the solar wind peak, are gyrating about the local magnetic field on the sunward and antisunward sides from the ion bulk velocity.

These distinct ion populations in the first half of the HFA are qualitatively consistent with our understanding of HFAs as kinetic phenomena. Collisionless, unmagnetized conditions preserve coherent phase-space features. It has not proven possible to link the individual features with sources before or after the intersection of the HFA leading edge with the nominal bow shock. The fall in density requires expansion (inferred from the wider perspective, see Table 1). Despite the apparent lack of coupling here, the fall in phase-space density requires dissipation.

Thus, the first half of the HFA interior is characterized by phase-space clumps of ions including both the incident solar wind and, probably, relics of shock-reflected ions. Overall, these features are distributed in the direction indicated by the white line (e.g., Figure 3A(b,e)), propagating upstream along and confined by the current sheet. However, they are moving sunward and southward with respect to that locus, and thus are unable to remain in step with the current sheet convection by the solar wind. This is consistent with the overall $V_z \sim +200$ km/s, less than the 470 km/s of V_{tr} (Table 1).

3.2. Ion Kinetics—Late Interior

The latter half of the HFA (Figure 3B) sweeps up particles unable to keep up with the current sheet convection. This region is denser with a stronger magnetic field, so that the gyroradius of a 1 keV proton, typical of the solar wind, falls below 1,000 km, 1/7th of the HFA half-width. The more energetic protons fill the backstreaming hemisphere along the current sheet. This also corresponds to the post-HFA magnetic field direction (thin magenta line) in Figure 3C.

The solar wind peak bifurcates in Figure 3B(h) connected by a crescent around the magnetic field direction (Figure 3D(h)). Judging by its displacement from the origin (the center of momentum), it must be balanced in inertia by the more diffuse population in the right half corresponding to ions traveling along the current sheet in Figure 3B(h). Thus, here there is sufficient backstreaming density to force the depleted solar wind peak into mutual gyration. There is also some relative field-aligned motion seen in E(h). This is evidence of a kinematic rather than turbulent coupling process, although the spread into a crescent may require some scattering in gyrophase.

There are still discreet features in the antisunward hemisphere from low to solar wind speeds. Two strong peaks appear in different orientations in Figure 3B(i,j). The larger of these is deflected southward, similar to that in the trailing edge compression region (Figure 3B(k)) which is the downstream *sheath* of the trailing shock. This flow drives the transverse expansion of the trailing edge. Figure 3D(i) shows that the smaller peak is gyrating around the larger one.

Finally, we note that the diffuse sunward-streaming population within the HFA is not organized by the local magnetic field, but in general fills the locus bounded by the post-HFA 90° pitch angle curve, cf., Figure 3C(i). While it is tempting to suggest that these ions have their source in the post-HFA quasi-parallel foreshock (Omidi & Sibeck, 2007), the post-HFA field-aligned backstreaming ions (e.g., C(l)) are far less intense than the ions found within the HFA. It is possible that they have the same or similar source, but that the interaction with the HFA, seen in the overall compression from leading to trailing edge, enhances their intensity. If so, they need to circumvent the trailing edge sheath, where their intensity is already close that seen in the post-HFA solar wind.

Thus, the latter half of the HFA is characterized by an overall increase in ion density and a compactification of the phase-space distribution. There remain distinct nongyrotropic ion features that, in the larger magnetic fields found here, gyrate around their mutual center of momentum. This represents a coherent, kinematic coupling between the incident, antisunward ions and those backstreaming from the bow shock, magnetosheath, or even internal HFA regions.

3.3. Alpha Particles

The small, broken signal at twice the solar wind energy per charge seen pre- and post-HFA in Figure 1a are solar wind alphas. The HPCA instrument discriminates species and Figure 1c shows the alpha particle spectrogram. HPCA accumulates azimuths over a half spin (10 s). Thus, the narrow solar wind alpha peak persists within the HFA interior as the small bright repeating feature, weakening in intensity within the HFA. It is accompanied by a more energetic alpha particle population that fills all azimuths (i.e., is present at all times) within the HFA, growing more intense toward the latter half of the HFA in common with the protons discussed above. Prior to entry into the trailing compression region, the alpha peak lowers in energy and is accompanied by a second narrow alpha population at even lower energies. As these two populations are observed at roughly the same time, they are at similar flow azimuths, corresponding to antisunward flow. They may contribute to the ions seen in Figure 3B(j). Together with the more diffuse alpha population this confirms that the solar wind alphas also participate in HFA dynamics and heating (Galvez et al., 1990) evidenced by deceleration, bifurcation, and diffuse components.

4. Summary

Using high resolution MMS observations, we probed ion kinetic signatures of a HFA. In the canonical HFA model (Burgess, 1989; Burgess & Schwartz, 1988; Omidi & Sibeck, 2007), the interaction of an interplanetary current sheet with the bow shock results, under suitable conditions, in reflected ions being channeled upstream along the current sheet where they couple with the solar wind beam. A resulting instability is then responsible for the strongly deflected, hot, and nearly Maxwellian interior of mature HFAs (Thomsen et al., 1988; Zhang et al., 2010).

On the other hand, Vaisberg et al. (2016) studied a young HFA in which the solar wind beam is distinct. They suggested that the hot interior region in their event was the nominal magnetosheath plasma protruding into the upstream region.

The HFA studied here has not evolved into a nearly Maxwellian state. The first half of the HFA retains a peak at the nominal solar wind ion energy, but reduced in density (and phase-space density) well below what would be expected from a 2-D transverse expansion. We identified distinct groups of ions with velocities roughly aligned with the current sheet and propagating sunward with respect to the incident flow.

Deeper in the HFA, the solar wind component increases in density, while the backstreaming ions form distinct groups including both narrow sunward moving ions and broader backstreaming distributions unable to keep pace with the convecting current sheet. These particles drift toward the trailing edge of the HFA. We attribute the smooth increase in density throughout the HFA interior to such ions being swept up by the strongly compressed trailing edge.

The latter half of the HFA shows sufficient magnetic field compression to render ions of solar wind energies magnetized. However, the more diffuse, energetic backstreaming ions are not organized by the local magnetic field but instead fill a velocity-space hemisphere reminiscent of the current sheet and/or post-HFA interplanetary magnetic field. The dominant antisunward population is stretched into a velocity-space crescent, or appears as two distinct peaks. Analysis reveals that the different ion populations are in mutual gyration around their common center of momentum.

Thus, despite the presence of high amplitude bulk velocity fluctuations, this resolved gyration reveals a coherent coupling process between the incident and backstreaming ion populations. While we are not able to follow individual ions to their sources, the discreet, multicomponent nature of the ion populations and their location in velocity space are consistent with the generic HFA theory of the channeling of reflected particles.

Some of the ion distributions are also reminiscent of contributions by preexisting backstreaming ions (Vaisberg et al., 2016). Simulations (Omidi & Sibeck, 2007) suggest that in circumstances in which one side of the current sheet connects to the quasi-parallel bow shock, the HFA tends to form on that side. That is nearly the case here, although the post-HFA geometry is somewhat oblique ($\theta_{Bn} \sim 54^\circ$). While we have shown that post-HFA field orientation is indeed consistent with the structure of the backstreaming diffuse population within the latter stages of the HFA, those ions are far more intense than the foreshock beam of ions found immediately on exiting the HFA.

5. Conclusions

We have explored kinetic aspects of the structure within a HFA observed near Earth's bow shock. The high-cadence MMS FPI plasma measurements reveal fine, unalised signatures in ion velocity-space. Despite the high level of fluctuations, these signatures show a systematic evolution from one edge of the HFA to the other.

Unlike mature HFAs with hot near-Maxwellian cores, this HFA retains a peak in phase-space at/near the incident solar wind together with backstreaming clumps or diffuse ions which drift toward the HFA trailing edge. The incident and backstreaming populations couple kinematically through their mutual gyration about the center of momentum rather than some more turbulent process.

Further work will explore the impact of solar wind alpha particles, which are shown here to display some of the same characteristics including a persistent diffuse backstreaming population and eventual deceleration/deflection. The electrons support large-amplitude fluctuations within the HFA (see supporting information S1); their kinetic characteristics are worthy of a separate investigation.

Acknowledgments

S.J.S. held a Leverhulme Research Fellowship hosted by LASP. We note with sadness the death of our colleague, Jack Gosling, who was involved in the early stages of the manuscript. MMS is a NASA-funded mission. MMS data is publicly available at the Science Data Center (<https://lasp.colorado.edu/mms/sdc/public/>). WIND data were drawn from CDAWeb (cdaweb.sci.gsfc.nasa.gov) and provided by A. Szabo, R. Lin, S. Bale, and K. Ogilvie. Partial support included UK/STFC grant ST/N000692/1 (S.J.S., J.P.E.); NSF AGS-1352669 (HZ).

References

- Burch, J. L., Moore, T. E., Torbert, R. B., & Giles, B. L. (2016). Magnetospheric multiscale overview and science objectives. *Space Science Reviews*, 199, 5–21. <https://doi.org/10.1007/s11214-015-0164-9>
- Burgess, D. (1989). On the effect of a tangential discontinuity on ions specularly reflected at an oblique shock. *Journal of Geophysical Research*, 94, 472–478. <https://doi.org/10.1029/JA094iA01p00472>
- Burgess, D., & Scholer, M. (2015). *Collisionless shocks in space plasmas: Structure and accelerated particles*. Cambridge, UK: Cambridge University Press.
- Burgess, D., & Schwartz, S. J. (1988). Colliding plasma structures: Current sheet and perpendicular shock. *Journal of Geophysical Research*, 93, 11,327–11,340. <https://doi.org/10.1029/JA093iA10p11327>
- Collinson, G., Halekas, J., Grebowsky, J., Connerney, J., Mitchell, D., Espley, J., & Jakosky, B. (2015). A hot flow anomaly at Mars. *Geophysical Research Letters*, 42, 9121–9127. <https://doi.org/10.1002/2015GL065079>
- Collinson, G. A., Sibeck, D. G., Masters, A., Shane, N., Slavin, J. A., Coates, A. J., & Barabash, S. (2012). Hot flow anomalies at Venus. *Journal of Geophysical Research*, 117, A04204. <https://doi.org/10.1029/2011JA017277>
- Collinson, G. A., Sibeck, D. G., Masters, A., Shane, N., Zhang, T. L., Fedorov, A., & Sarantos, M. (2014). A survey of hot flow anomalies at Venus. *Journal of Geophysical Research: Space Physics*, 119, 978–991. <https://doi.org/10.1002/2013JA018863>
- Dunlop, M. W., & Woodward, T. I. (1998). Multi-spacecraft discontinuity analysis: Orientation and motion. *ISSI Scientific Reports Series*, 1, 271–306.
- Eastwood, J. P., Schwartz, S. J., Horbury, T. S., Carr, C. M., Glassmeier, K. H., Richter, I., & Wild, J. A. (2011). Transient Pc3 wave activity generated by a hot flow anomaly: Cluster, Rosetta, and ground-based observations. *Journal of Geophysical Research*, 116, A08224. <https://doi.org/10.1029/2011JA016467>
- Eastwood, J. P., Sibeck, D. G., Angelopoulos, V., Phan, T. D., Bale, S. D., McFadden, J. P., & Le Contel, O. (2008). THEMIS observations of a hot flow anomaly: Solar wind, magnetosheath, and ground-based measurements. *Geophysical Research Letters*, 35, L17S03. <https://doi.org/10.1029/2008GL033475>
- Ergun, R. E., Tucker, S., Westfall, J., Goodrich, K. A., Malaspina, D. M., Summers, D., & Cully, C. M. (2016). The axial double probe and fields signal processing for the MMS mission. *Space Science Reviews*, 199, 167–188. <https://doi.org/10.1007/s11214-014-0115-x>
- Facsó, G., Kecskeméty, K., Erdős, G., Tátrallyay, M., Daly, P. W., & Dandouras, I. (2008). A statistical study of hot flow anomalies using Cluster data. *Advances in Space Research*, 41, 1286–1291. <https://doi.org/10.1016/j.asr.2008.02.005>
- Facsó, G., Németh, Z., Erdos, G., Kis, A., & Dandouras, I. (2009). A global study of hot flow anomalies using Cluster multi-spacecraft measurements. *Annals of Geophysics*, 27, 2057–2076. <https://doi.org/10.5194/angeo-27-2057-2009>
- Fazakerley, A. N., Schwartz, S. J., & Paschmann, G. (1998). Measurement of plasma velocity distributions. *ISSI Scientific Reports Series*, 1, 91–124.
- Fuselier, S. A., Thomsen, M. F., Gosling, J. T., Bame, S. J., & Russell, C. T. (1987). Fast shocks at the edges of hot diamagnetic cavities upstream from the Earth's bow shock. *Journal of Geophysical Research*, 92, 3187–3194. <https://doi.org/10.1029/JA092iA04p03187>
- Galvez, M., Fuselier, S. A., Gary, S. P., Thomsen, M. F., & Winske, D. (1990). Alpha particle heating in hot diamagnetic cavities. *Journal of Geophysical Research*, 95, 11,975–11,982. <https://doi.org/10.1029/JA095iA08p11975>
- Gershman, D. J., Avakov, L. A., Boardsen, S. A., Dorelli, J. C., Gliese, U., Barrie, A. C., & Pollock, C. J. (2017). Spacecraft and instrument photoelectrons measured by the Dual Electron Spectrometers on MMS. *Journal of Geophysical Research: Space Physics*, 122, 11,548–11,558. <https://doi.org/10.1002/2017JA024518>
- Harteringer, M. D., Turner, D. L., Plaschke, F., Angelopoulos, V., & Singer, H. (2013). The role of transient ion foreshock phenomena in driving Pc5 ULF wave activity. *Journal of Geophysical Research: Space Physics*, 118, 299–312. <https://doi.org/10.1029/2012JA018349>
- Kovács, P., Facsó, G., & Dandouras, I. (2014). Turbulent dynamics inside the cavity of hot flow anomaly. *Planetary and Space Science*, 92, 24–33. <https://doi.org/10.1016/j.pss.2014.01.001>
- Lin, R. P., Anderson, K. A., Ashford, S., Carlson, C., Curtis, D., Ergun, R., & Paschmann, G. (1995). A three-dimensional plasma and energetic particle investigation for the wind spacecraft. *Space Science Reviews*, 71, 125–153. <https://doi.org/10.1007/BF00751328>
- Lindqvist, P. A., Olsson, G., Torbert, R. B., King, B., Granoff, M., Rau, D., & Tucker, S. (2016). The spin-plane double probe electric field instrument for MMS. *Space Science Reviews*, 199, 137–165. <https://doi.org/10.1007/s11214-014-0116-9>
- Liu, T. Z., Angelopoulos, V., & Hietala, H. (2017). Energetic ion leakage from foreshock transient cores. *Journal of Geophysical Research: Space Physics*, 122, 7209–7225. <https://doi.org/10.1002/2017JA024257>
- Liu, T. Z., Turner, D. L., Angelopoulos, V., & Omid, N. (2016). Multipoint observations of the structure and evolution of foreshock bubbles and their relation to hot flow anomalies. *Journal of Geophysical Research: Space Physics*, 121, 5489–5509. <https://doi.org/10.1002/2016JA022461>

- Lucek, E. A., Horbury, T. S., Balogh, A., Dandouras, I., & Rème, H. (2004). Cluster observations of hot flow anomalies. *Journal of Geophysical Research*, *109*, A06207. <https://doi.org/10.1029/2003JA010016>
- Masters, A., Arridge, C. S., Dougherty, M. K., Bertucci, C., Billingham, L., Schwartz, S. J., & Thomsen, M. F. (2008). Cassini encounters with hot flow anomaly-like phenomena at Saturn's bow shock. *Geophysical Research Letters*, *35*, L02202. <https://doi.org/10.1029/2007GL032371>
- Masters, A., McAndrews, H. J., Steinberg, J. T., Thomsen, M. F., Arridge, C. S., Dougherty, M. K., & Coates, A. J. (2009). Hot flow anomalies at Saturn's bow shock. *Journal of Geophysical Research*, *114*, A08217. <https://doi.org/10.1029/2009JA014112>
- Omidi, N., & Sibeck, D. G. (2007). Formation of hot flow anomalies and solitary shocks. *Journal of Geophysical Research*, *112*, A01203. <https://doi.org/10.1029/2006JA011663>
- Onsager, T. G., Thomsen, M. F., & Winske, D. (1990). Hot flow anomaly formation by magnetic deflection. *Geophysical Research Letters*, *17*, 1621–1624. <https://doi.org/10.1029/GL017i010p01621>
- Paschmann, G., Haerendel, G., Sckopke, N., Moebius, E., & Luehr, H. (1988). Three-dimensional plasma structures with anomalous flow directions near the Earth's bow shock. *Journal of Geophysical Research*, *93*, 11,279–11,294. <https://doi.org/10.1029/JA093iA10p11279>
- Paschmann, G., Schwartz, S., Escoubet, C., & Haaland, S. (2005). *Outer magnetospheric boundaries: Cluster results*. Berlin: Springer.
- Pollock, C., Moore, T., Jacques, A., Burch, J., Gliese, U., & Saito, Y. (2016). Fast plasma investigation for magnetospheric multiscale. *Space Science Reviews*, *199*, 331–406. <https://doi.org/10.1007/s11214-016-0245-4>
- Russell, C. T., Anderson, B. J., Baumjohann, W., Bromund, K. R., Dearborn, D., Fischer, D., et al. (2016). The magnetospheric multiscale magnetometers. *Space Science Reviews*, *199*, 189–256. <https://doi.org/10.1007/s11214-014-0057-3>
- Schwartz, S. J. (1998). Shock and discontinuity normals, Mach numbers, and related parameters. *ISSI Scientific Reports Series*, *1*, 249–270.
- Schwartz, S. J., Chaloner, C. P., Hall, D. S., Christiansen, P. J., & Johnstone, A. D. (1985). An active current sheet in the solar wind. *Nature*, *318*, 269–271. <https://doi.org/10.1038/318269a0>
- Schwartz, S. J., Kessel, R. L., Brown, C. C., Woolliscroft, L. J. C., & Dunlop, M. W. (1988). Active current sheets near the Earth's bow shock. *Journal of Geophysical Research*, *93*, 11,295–11,310. <https://doi.org/10.1029/JA093iA10p11295>
- Schwartz, S. J., Paschmann, G., Sckopke, N., Bauer, T. M., Dunlop, M., Fazakerley, A. N., & Thomsen, M. F. (2000). Conditions for the formation of hot flow anomalies at Earth's bow shock. *Journal of Geophysical Research*, *105*, 12,639–12,650. <https://doi.org/10.1029/1999JA000320>
- Shestakov, A. Y., & Vaisberg, O. L. (2016). Study and comparison of the parameters of five hot flow anomalies at a bow shock front. *Cosmic Research*, *54*, 77–95. <https://doi.org/10.1134/S0010952516020064>
- Sibeck, D. G., Borodkova, N. L., Schwartz, S. J., Owen, C. J., Kessel, R., Kokubun, S., & Zastenker, G. N. (1999). Comprehensive study of the magnetospheric response to a hot flow anomaly. *Journal of Geophysical Research*, *104*, 4577–4594. <https://doi.org/10.1029/1998JA900021>
- Sibeck, D. G., Kudela, K., Lepping, R. P., Lin, R., Nemecek, Z., Nozdachev, M. N., & Yermolaev, Y. (2000). Magnetopause motion driven by interplanetary magnetic field variations. *Journal of Geophysical Research*, *105*, 25,155–25,170. <https://doi.org/10.1029/2000JA900109>
- Slavin, J. A., & Holzer, R. E. (1981). Solar wind flow about the terrestrial planets. I - Modeling bow shock position and shape. *Journal of Geophysical Research*, *86*, 11,401–11,418. <https://doi.org/10.1029/JA086iA13p11401>
- Thomsen, M. F., Gosling, J. T., Bame, S. J., Quest, K. B., & Russell, C. T. (1988). On the origin of hot diamagnetic cavities near the Earth's bow shock. *Journal of Geophysical Research*, *93*, 11,311–11,325. <https://doi.org/10.1029/JA093iA10p11311>
- Thomsen, M. F., Gosling, J. T., Fuselier, S. A., Bame, S. J., & Russell, C. T. (1986). Hot, diamagnetic cavities upstream from the Earth's bow shock. *Journal of Geophysical Research*, *91*, 2961–2973. <https://doi.org/10.1029/JA091iA03p02961>
- Thomsen, M. F., Thomas, V. A., Winske, D., Gosling, J. T., Farris, M. H., & Russell, C. T. (1993). Observational test of hot flow anomaly formation by the interaction of a magnetic discontinuity with the bow shock. *Journal of Geophysical Research*, *98*, 15,319–15,330. <https://doi.org/10.1029/93JA00792>
- Torbert, R. B., Russell, C. T., Magnes, W., Ergun, R. E., Lindqvist, P. A., LeContel, O., & Lappalainen, K. (2016). The FIELDS instrument suite on MMS: Scientific objectives, measurements, and data products. *Space Science Reviews*, *199*, 105–135. <https://doi.org/10.1007/s11214-014-0109-8>
- Tsurutani, B. T., & Stone, R. G. (1985). *Collisionless shocks in the heliosphere: Reviews of current research*. Washington, DC: American Geophysical Union. <https://doi.org/10.1029/GM035>
- Turner, D. L., Wilson, L. B., Liu, T. Z., Cohen, I. J., Schwartz, S. J., Osmane, A., & Burch, J. L. (2018). Autogenous and efficient acceleration of energetic ions upstream of Earth's bow shock. *Nature*, *561*(7722), 206–210. <https://doi.org/10.1038/s41586-018-0472-9>
- Uritsky, V. M., Slavin, J. A., Boardsen, S. A., Sundberg, T., Raines, J. M., Gershman, D. J., & Korth, H. (2014). Active current sheets and candidate hot flow anomalies upstream of Mercury's bow shock. *Journal of Geophysical Research: Space Physics*, *119*, 853–876. <https://doi.org/10.1002/2013JA019052>
- Vaisberg, O. L., Shuvalov, S. D., Shestakov, A. Y., & Golubeva, Y. M. (2016). Origin of the backstreaming ions in a young Hot Flow Anomaly. *Planetary and Space Science*, *131*, 102–110. <https://doi.org/10.1016/j.jpsp.2016.08.003>
- Valek, P. W., Thomsen, M. F., Allegrini, F., Bagenal, F., Bolton, S., Connerney, J., & Wilson, R. J. (2017). Hot flow anomaly observed at Jupiter's bow shock. *Geophysical Research Letters*, *44*, 8107–8112. <https://doi.org/10.1002/2017GL073175>
- Wang, S., Zong, Q., & Zhang, H. (2013). Hot flow anomaly formation and evolution: Cluster observations. *Journal of Geophysical Research: Space Physics*, *118*, 4360–4380. <https://doi.org/10.1002/jgra.50424>
- Young, D. T., Burch, J. L., Gomez, R. G., De Los Santos, A., Miller, G. P., Wilson, P., & Webster, J. M. (2016). Hot plasma composition analyzer for the magnetospheric multiscale mission. *Space Science Reviews*, *199*, 407–470. <https://doi.org/10.1007/s11214-014-0119-6>
- Zhang, H., Sibeck, D. G., Zong, Q. G., Gary, S. P., McFadden, J. P., Larson, D., & Angelopoulos, V. (2010). Time history of events and macroscale interactions during substorms observations of a series of hot flow anomaly events. *Journal of Geophysical Research*, *115*, A12235. <https://doi.org/10.1029/2009JA015180>
- Zhao, L. L., Zhang, H., & Zong, Q. G. (2017a). Global ULF waves generated by a hot flow anomaly. *Geophysical Research Letters*, *44*, 5283–5291. <https://doi.org/10.1002/2017GL073249>
- Zhao, L. L., Zhang, H., & Zong, Q. G. (2017b). A statistical study on hot flow anomaly current sheets. *Journal of Geophysical Research: Space Physics*, *122*, 235–248. <https://doi.org/10.1002/2016JA023319>